AGU PUBLICATIONS

JGR

Journal of Geophysical Research: Solid Earth

RESEARCH ARTICLE

10.1002/2013JB010781

**Key Points:**
- Anisotropic model beneath eastern China
- Mapping the boundary of the craton
- Geodynamical interpretations

**Correspondence to:**
C. P. Legendre,
legendre@earth.sinica.edu.tw

**Citation:**
Legendre, C. P., F. Deschamps, L. Zhao, S. Lebedev, and Q.-F. Chen (2014), Anisotropic Rayleigh wave phase velocity maps of eastern China, *J. Geophys. Res. Solid Earth*, *119*, 4802–4820, doi:10.1002/2013JB010781.

Received 17 OCT 2013
Accepted 14 MAY 2014
Accepted article online 17 MAY 2014
Published online 2 JUN 2014

# Anisotropic Rayleigh wave phase velocity maps of eastern China

**C. P. Legendre[1], F. Deschamps[1], L. Zhao[1], S. Lebedev[2], and Q.-F. Chen[3]**

[1]Institute of Earth Sciences, Academia Sinica, Taipei, Taiwan, [2]Geophysics Section, Dublin Institute for Advanced Studies, Dublin, Ireland, [3]Key Laboratory of the Earth's Deep Interior, Institute of Geology and Geophysics, Chinese Academy of Sciences, Beijing, China

**Abstract** We explore the variations of Rayleigh wave phase velocity beneath eastern China in a broad period range (20–200 s). Rayleigh wave dispersion curves are measured by the two-station technique for a total of 734 interstation paths using vertical component broadband waveforms at 39 seismic stations in eastern China from 466 global earthquakes. In addition, 599 waveform inversion interstation measurements were added to this data set. The interstation dispersion curves are then inverted for high-resolution isotropic and azimuthally anisotropic phase velocity maps at periods between 20 and 200 s. At shorter periods sampling the crustal depth range, phase velocities are higher in the southeastern part of the region, reflecting the thinner crust there. The Jiangnan Belt separates Cathaysia from the Yangtze Craton, the latter with thicker crust and a deep, high-velocity cratonic root. The eastern part of Yangtze Craton, however, east of 115–116°E, does not display a deep root and has a thin lithosphere. Azimuthal anisotropy at long periods (>120 s) shows fast propagation directions broadly similar to that of the absolute plate motion. Beneath Cathaysia and eastern Yangtze Craton, anisotropy in the asthenosphere is strong and suggests coast-perpendicular flow. Asthenospheric flow from beneath China's thick continental lithosphere toward the thinner lithosphere of the margin and the resulting decompression melting may be the fundamental causes of the intraplate basaltic volcanism along the eastern coast of China.

## 1. Introduction

The tectonic structure of China is strongly influenced by the collision between Eurasia and India. After the closure of the paleo-Pacific and Thetys Oceans, the collision of India with Asia led to the formation of the Tibetan Plateau. This major orogeny dominates the region today [*Bird*, 2003]; models for the mechanism of the continental convergence range from continental subduction to extrusion of the eastern margin of Tibet and parts of SE Asia [*Tapponnier et al.*, 1986; *Avouac and Tapponnier*, 1993; *Agius and Lebedev*, 2013]. Central and eastern China (i.e., east of the Tibetan Plateau), on which we focus in the present study, has formed in earlier continental collisions, record of which is preserved in the crustal and mantle structure [*Yin and Harrison*, 2000; *He and Tsukuda*, 2003] (Figure 1). The region may be split into north and south tectonic blocks [*He and Tsukuda*, 2003]. The boundary between these two blocks runs roughly in the EW direction at a latitude of 32°N. The north tectonic block is usually referred to as the Sino-Korean Craton (or North China Craton (NCC)), whereas the south tectonic block (or South China Block (SCB)) contains the Yangtze Craton. These tectonic provinces are bordered in the central part by two plain regions: the North China Plain and Hehuai Plain block [*Deng et al.*, 2003; *Jiang et al.*, 2013].

Tomographic models of Tibet [*Yao et al.*, 2006; *Zhang et al.*, 2011] confirmed that the Moho beneath Tibetan Plateau is deep (60–80 km depth). Latest studies also revealed a complex deformation, affecting the whole region, as seen in the tomographic images for the Sichuan-Yunnan Basin [*Lü et al.*, 2013]. The tectonics of the NCC is affected by the Tibetan orogeny in the west [*Yin and Harrison*, 2000; *He and Tsukuda*, 2003], while in the east the lithosphere of an Archean core of the craton has been thinned in the Phanerozoic [*Menzies and Xu*, 1998]. The NCC is composed of several uplifted blocks, high plains, and basins [*Zhao et al.*, 2001]. The SCB (Figure 1) includes, in its continental margin parts, Mesozoic magmatic provinces with volcanism between the Triassic and the Cretaceous [*Zhou et al.*, 2012; *Meng et al.*, 2012]. The presence of Jurassic granitoids distributed in a NE-SW elongated region (Nanling Range) as well as Neogene and Paleogene volcanism provides important clues on the evolution of the south China continental margin [*Li et al.*, 2012; *Yao et al.*, 2012]. *Chen et al.* [1981] first described the tectonic units in southern China, including Cathaysia Unit and Jiangnan Belt. Their formation and evolution were later detailed by geochemical evidences [*Chen and Jahn*,

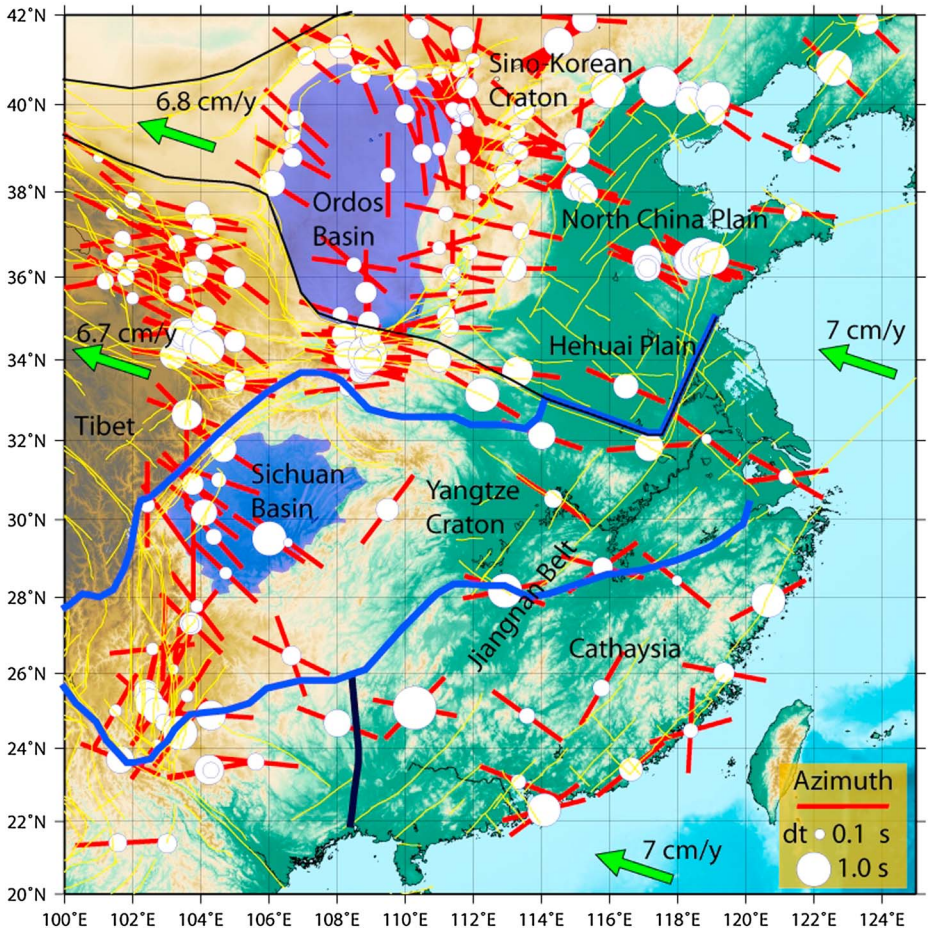


**Figure 1.** Azimuthal anisotropy in eastern China from shear-wave (SKS) splitting (modified from *Wüstefeld et al.* [2009]). The plate motions are taken from NUVEL1 model [*DeMets et al.*, 1990, 1994]. Ordos and Sichuan Basins are highlighted in blue, as well as the outline of the Yangtze Craton and Cathaysia Unit. The northern boundary of the Yangtze Craton is the limit between northern and southern China Tectonic Provinces [*He and Tsukuda*, 2003]. The complex fault system is plotted in yellow lines, and Jiangnan Belt is indicated.

1998; *Zhang et al.*, 2013]. The Yangtze Craton is surrounded by many active faults (Figure 1) but appears unaffected by tectonic activities and has experienced very weak deformation. Jiaoliao Plain is surrounded by several uplifted blocks (Taihangshan uplift) and mountains (Yingshan-Yanshan folded mountain). Two main basins (Ordos and Sichuan, the Archean cores of the Sino-Korean and Yangtze Cratons, respectively) and major faulting system (Tancheng-Lujiang fault) are also present in the region. In addition, the Cathaysia protocratonic unit in the southeast and the Yangtze Craton are separated by the Jiangnan orogenic belt. Surface wave tomographic models of *Zheng et al.* [2008] imaged the basins at periods between 10 and 30 s and show a crustal thickening from east to west in the region. These results were confirmed by shear wave measurements [*Sun et al.*, 2010] and ambient noise tomography [*Zhou et al.*, 2012]. The crustal structure [*Ma and Zhou*, 2007] is very heterogeneous with strong lateral variations, as confirmed by gravity measurements [*Li and Yang*, 2011]. Overall, however, the detailed interactions between the Yangtze Craton, the Sino-Korean Craton, and the Tibetan Plateau, as well as the border between the cratonic units and basins, are still poorly understood and call for further investigations.

Despite the large number of tomographic studies of the Asian upper mantle, the structure is still resolved unevenly with a typical resolution of hundreds of kilometers given by regional and global imaging [*Inoue et al.*, 1990; *Bijwaard et al.*, 1998; *Friederich*, 2003; *Lebedev and Nolet*, 2003; *Li et al.*, 2006; *Pei et al.*, 2007; *Zheng et al.*, 2008; *Sun et al.*, 2010; *Zhou et al.*, 2012; *Schaeffer and Lebedev*, 2013].

For models based on surface wave data, the resolution generally decreases with depth [*Lebedev et al.*, 2005; *Legendre et al.*, 2012; *Knapmeyer-Endrun et al.*, 2013]. Furthermore, lateral and radial resolution of the

models may vary strongly depending on the input data types. In most isotropic tomographic models, the large-scale anomalies are consistently resolved, such as the cratons (North China, Siberian, Yangtze), the Tibetan Plateau, and the subduction zones of the Western Pacific and Southeast Asia. Local-scale tomographic studies provide more details in the shape of the slabs and the boundaries of the cratons and the basins. Additional seismic imaging, in particular for the anisotropic structure, is, however, required to better understand the lithosphere-asthenosphere system in the Asian upper mantle, the internal structure of the cratonic mantle lithosphere as well as details of the cratons' boundaries with younger oceanic and continental units. Azimuthal anisotropy is of great importance to infer past and present deformation in the lithosphere and asthenosphere and can be retrieved by studying either the splitting of seismic shear waves (mainly S and SnKS), or the azimuthal dependence of body or surface wave speeds. Several SKS studies have been performed in the region (see *Wüstefeld et al.* [2009] for a review).

Shear wave splitting measurements reveal the presence of small-scale seismic anisotropy in the mantle in the region (Figure 1). The most striking result is the clear difference in fast direction of propagation around the Ordos and Sichuan Basins as well as in the western border of the Yangtze Craton. However, the fast directions are uniform inside the cratons with almost no variation in the fast direction of the anisotropy, except at the border of the cratonic units. One may point out that the WSW direction of the fast axis can be related to the absolute plate motion (NUVEL1 model, *DeMets et al.* [1990, 1994]). However, SKS measurements provide an average anisotropy across the whole crust and upper mantle and cannot precisely locate the depth range in which the anisotropy occurs. Because the vertical resolution of anisotropy is missing, it is not possible to discuss structural details. The variation of anisotropy with depth has increasingly been revealed by recent surface wave observations, sometimes in combination with shear wave splitting data [e.g., *Lebedev et al.*, 2006, 2009; *Deschamps et al.*, 2008a, 2008b; *Yuan and Romanowicz*, 2010; *Endrun et al.*, 2011; *Xie et al.*, 2013].

In this study, we construct anisotropic maps of Rayleigh wave phase velocity in east China (24°N–40°N and 104°E–120°E). We analyze the azimuthal patterns of Rayleigh wave phase velocity in several distinct period ranges and investigate the vertical as well as lateral variations of Rayleigh wave azimuthal anisotropy. At periods sampling the lower crust and the lithosphere, our results provide evidence for fossil fabric characterizing ancient deformation within cratonic lithosphere and the more recent mantle flow between the northern and southern regions of east China. At longer periods, where the surface waves mainly sample the asthenosphere, our results are broadly consistent with the absolute plate motion (APM) in this region [*DeMets et al.*, 1990, 1994].

## 2. Seismic Data and Methodology

We follow the conventional two-station approach in constructing the Rayleigh wave phase velocity maps in eastern China. First, we make phase velocity measurements using broadband waveform records and determine the interstation dispersion curves. We then invert the obtained collection of dispersion curves for Rayleigh wave phase velocity maps at selected periods between 20 and 200 s.

### 2.1. Seismic Stations and Selected Earthquakes

To measure the Rayleigh wave phase velocities beneath east China (roughly 24°N–40°N and 104°E–120°E), we use the broadband waveforms recorded at 39 seismic stations from the China National Seismic Network [*Zheng et al.*, 2010]. The stations are evenly distributed in our study region (Figure 2). The two-station method, which we employ to measure the dispersion curves between two stations using Rayleigh waves from earthquakes, requires that the angle between the great circles connecting a given pair of stations and that connecting this pair and the earthquake epicenter are small. In this study, we set an upper limit of 10° for this angle in the selection of earthquakes and station pairs. Epicentral distances are between 10° and 170°, and all interstation distances are in the range of 250–2500 km. Following these criteria, we extracted 59,306 records for 466 events (Figure 3). For each given pair of stations, all phase velocity measurements obtained from different earthquakes are averaged to derive the dispersion curve for the path connecting this pair of stations. This resulted in reliable dispersion curves for a total of 734 interstation paths.

### 2.2. Phase Velocity Dispersion Curves

For each of the 734 pairs of stations, we measured a phase velocity dispersion curve for the fundamental Rayleigh mode using the two-station method. This method was first introduced by *Sato* [1955] and has been used to measure dispersion curves of surface waves [*Schwab and Knopoff*, 1970; *Knopoff*, 1972].

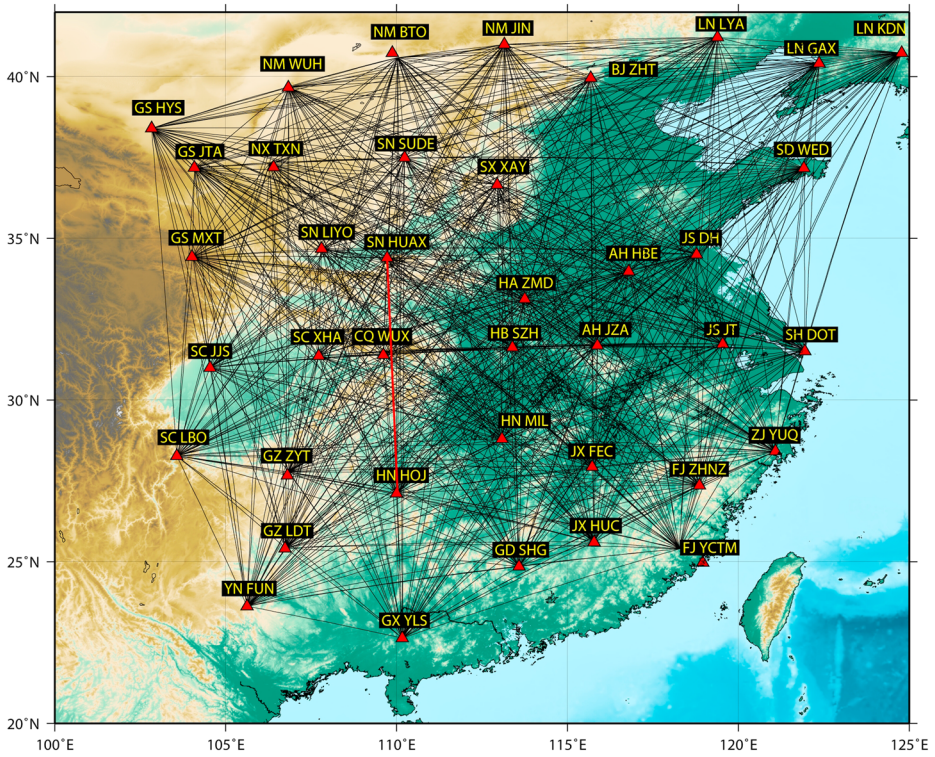


**Figure 2.** Stations (red triangles) used in this study plus station pairs used to constrain the model (black lines). The red interstation path is the one used, for example, in Figures 4–6.

Here we used the implementation of the cross-correlation approach of *Meier et al.* [2004], which allows measurements of dispersion curves in a broad period range (in our case, between 10 and 250 s). For each selected event, the vertical component displacements recorded at the two stations in each pair are cross correlated (Figure 4). To minimize the effects of noise and interferences, the cross-correlation function is first filtered with a Gaussian band-pass filter. Side lobes caused by correlations of the fundamental mode with scattered waves and higher modes are then downweighted by the application in the time domain of a frequency-dependent Gaussian window to the filtered cross-correlation

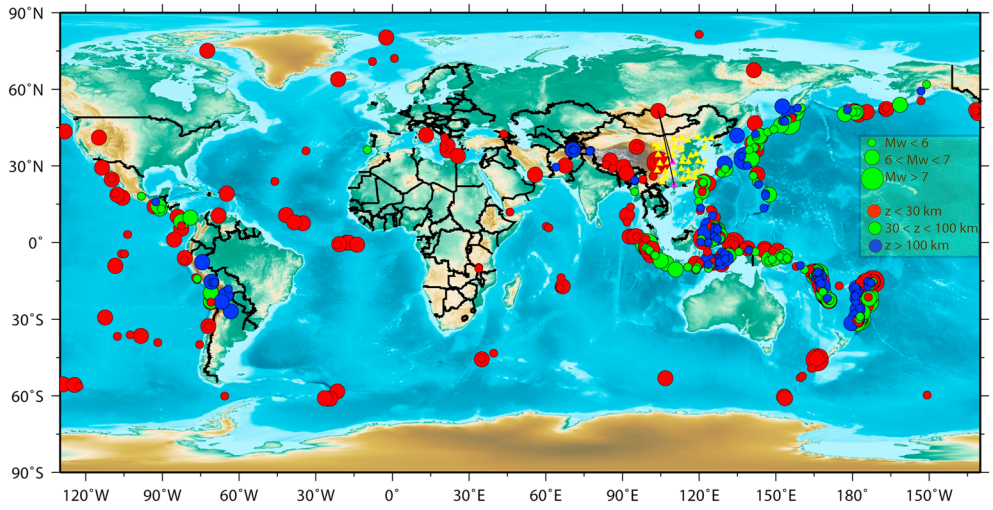


**Figure 3.** Events (circles) and stations (triangles) used in this study. The size of an event is related to the magnitude and the color to the event depth (shallow in red, up to 100 km depth in green, and deep in blue). A specific event is highlighted. The corresponding paths are shown in black lines, connected to the two stations in purple used, for example, in Figures 4–6.

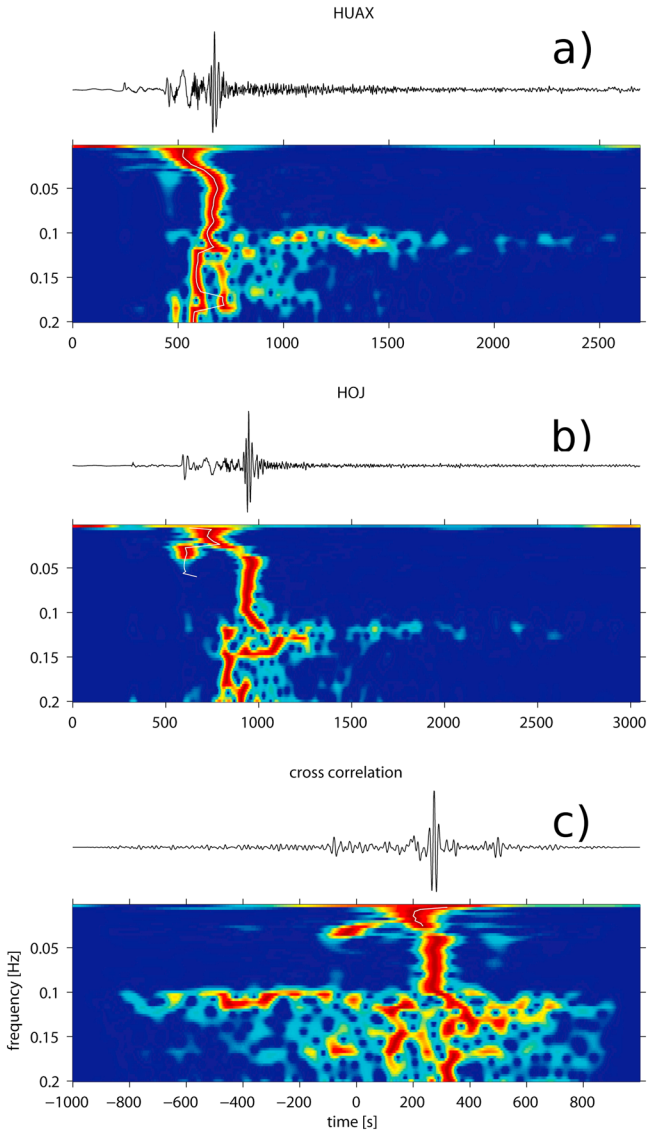


**Figure 4.** (a and b) Vertical components of the displacement recorded at the pair of stations highlighted in Figure 2 and (c) the cross-correlation function.

function. This approach to filtering and windowing is effective as long as the fundamental mode has the largest amplitude in the seismogram (which is usually true at epicentral distances greater than 1200 km, with the exception of seismograms from deep events) and therefore dominates the contribution to the cross-correlation function (Figure 4c).

The cross-correlation is then transferred into the frequency domain, and its complex phase $\zeta(\omega)$ is used to calculate the phase velocity C($\omega$) following

$$C(\omega) = \frac{\omega(\Delta_1 - \Delta_2)}{\zeta(\omega)}, \quad (1)$$

with

$$\zeta(\omega) = \arctan\left\{\frac{Im\,[\Phi(\omega)]}{Re\,[\Phi(\omega)]}\right\} + 2n\pi, \quad (2)$$

where $\Phi(\omega)$ is the transformed cross correlation between the surface waves recorded at the two stations with epicentral distances $\Delta_1$ and $\Delta_2$.

Because of the $2\pi$ ambiguity of the complex phase of the cross-correlation function (equation (2)), the phase velocity estimation is nonunique and is represented by an array of curves (blue curves in Figure 5). Phase velocity can be determined within a frequency range that is chosen interactively, and several nonoverlapping frequency ranges can be selected for one single event. Generally speaking, seismic wave diffraction and the interference of fundamental Rayleigh wave with

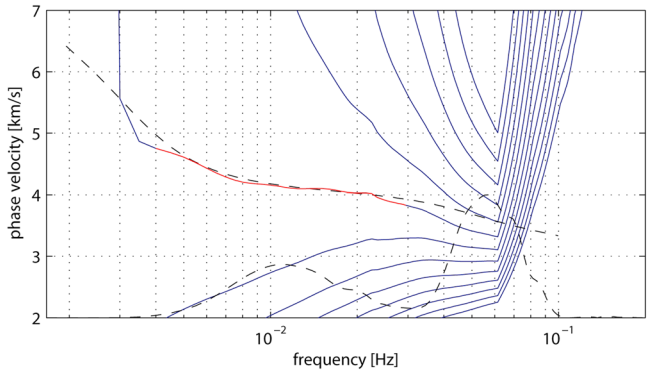


**Figure 5.** Possible solutions represented by an array of curves (blue lines). The model-predicted phase velocities for Rayleigh and Love waves are displayed in dashed line. The red part of the curve is the frequency window selected for this specific event.

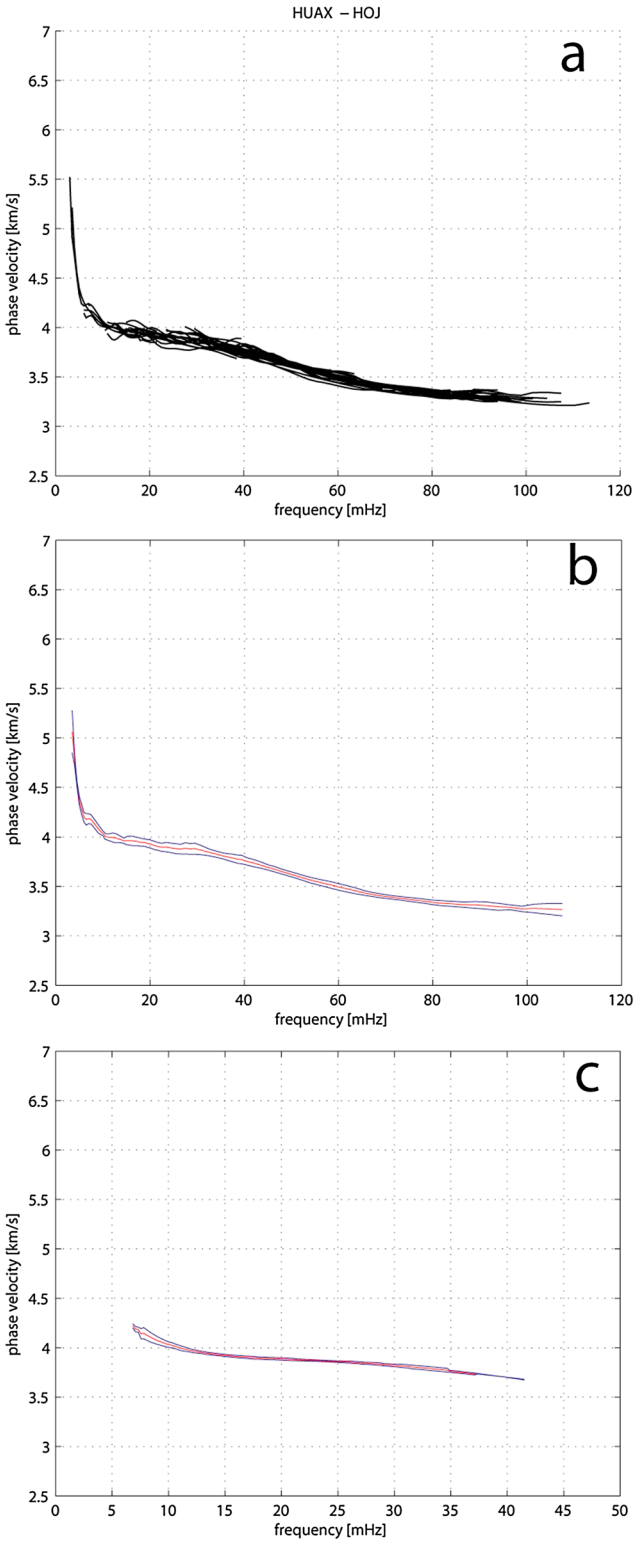


**Figure 6.** Dispersion curves for the pair HUAX-HOJ. (a) Measured phase velocity curves. (b) Merged curve. (c) Automated calculations to reduce the error in the final dispersion curve.

higher modes can bias the measurements. These effects, however, have a strong frequency dependence, which manifests itself in the irregularities and roughness in the measured curves. Therefore, only the smooth portions of the curve are retained (red portion in Figure 5). In the next step, all dispersion curves from the same station pair are merged together (Figure 6b), and outliers are discarded.

All the measurements from all available events selected at a specific pair of stations are then assembled and averaged to construct a single dispersion curve between the two stations. Merging all the segments of the dispersion curve measured for each event recorded at a given pair of station allows reaching a broader period range. At each period, the value of the Rayleigh wave phase velocity and its error bar are defined by the mean and standard deviation in the collection of the measured segments (red and blue lines in Figure 6b). In addition to the dispersion curves measured with the two-station method, automated measurements performed by the automated multimode inversion [*Lebedev et al.*, 2005] have been incorporated, as described in *Lebedev et al.* [2006]. A total of 599 path-specific dispersion curves have been added. The advantage of adding these measurements is to reduce the uncertainty on the dispersion curve: the automated measurements display a smaller standard deviation than the manually picked ones, although their frequency range does not extend to periods as short as for cross-correlation measurements (Figure 7).

To obtain the final dispersion curve, we take the average of manual and automated phase velocity measurements for the same interstation path. In general, the manually derived dispersion curves have larger errors but cover a broader range of frequencies. On the other hand, the automated multimode inversion operates over a more limited period range (with periods mostly over 20 s), but the resulting dispersion curves provide more accurate constrains on the phase velocity estimations. The standard deviation of the phase velocities measured at each period is a conservative estimate of the error in the dispersion curve. The errors generally increase with period, as shown in Figures 6b and 6c. The

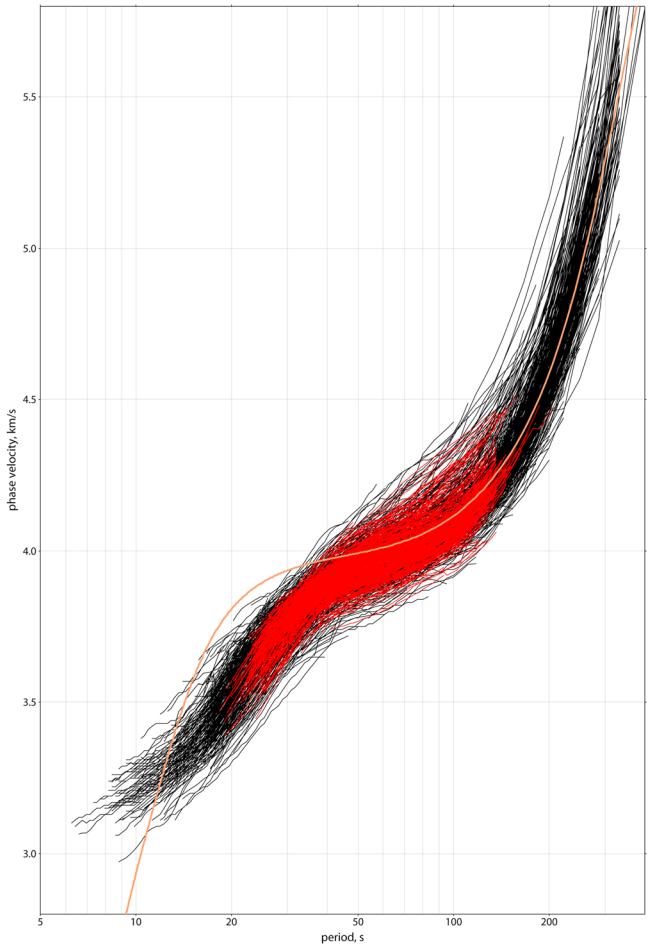


**Figure 7.** Manually measured phase velocity curves (black) and automated waveform inversion measurements (red) for all station pairs.

dispersion curves (obtained by merging manually picked and automated curves) we measured do not all cover the entire period range (10–250 s). As a result, the path coverage changes strongly with period (Figure 8), leading to variations in the resolution of our model as a function of period. For example, short periods (20 s and shorter) show relatively sparse coverage. By contrast, almost all the dispersion curves we obtained sample periods of 20 s and longer, leading to a very good coverage at these periods, as indicated by the azimuthal coverage for periods of 20 s and longer (Figure 8).

### 2.3. Inversion for Rayleigh Wave Phase Velocity Maps

After deriving the dispersion curves for the 734 interstation paths, we then invert them for both isotropic and anisotropic ($2\psi$ and $4\psi$) Rayleigh wave phase velocity maps at selected periods. At each point of the model, the total velocity anomaly can be parameterized with five coefficients: one coefficient for the isotropic phase velocity variation, $\delta C_{\text{iso}}$; two coefficients for the $2\psi$ anomaly, $A_{2\psi}$ and $B_{2\psi}$; and two coefficients for the $4\psi$ anomaly, $A_{4\psi}$ and $B_{4\psi}$:

$$\delta C = \delta C_{\text{iso}} + A_{2\psi} \times \cos(2\psi) + B_{2\psi} \times \sin(2\psi) + A_{4\psi} \times \cos(4\psi) + B_{4\psi} \times \sin(4\psi). \quad (3)$$

The amplitudes of azimuthal velocity variation ($\Lambda$) and the directions of fast propagation ($\Theta$) of the $2\psi$ and $4\psi$ anisotropy are then given by

$$\begin{cases} \Lambda_{2\psi} = \sqrt{A_{2\psi}^2 + B_{2\psi}^2} \\ \Theta_{2\psi} = \frac{1}{2} \arctan\left(\frac{B_{2\psi}}{A_{2\psi}}\right) \end{cases} \text{and} \begin{cases} \Lambda_{4\psi} = \sqrt{A_{4\psi}^2 + B_{4\psi}^2} \\ \Theta_{4\psi} = \frac{1}{4} \arctan\left(\frac{B_{4\psi}}{A_{4\psi}}\right). \end{cases} \quad (4)$$

Previous studies [*Montagner and Tanimoto*, 1991; *Trampert and Woodhouse*, 2003; *Polat et al.*, 2012] have pointed out that the contribution of $4\psi$ terms may be nonnegligible, which is why we have included them in our inversions. However, *Deschamps et al.* [2008a] found that although the $4\psi$ terms have amplitudes comparable to those of the $2\psi$ terms, they are not needed to explain the raw data. Therefore, in discussing inversion results in this study, we will not attempt to interpret the $4\psi$ terms and focus only on the isotropic and $2\psi$ anisotropic anomalies.

Geographically, the model is parameterized on a triangular grid of knots [*Wang and Dahlen*, 1995] with a grid spacing of 100 km. Due to uneven data coverage depending on the period, the size of the grid is different at each period. Best coverage (which is obtained for periods longer than 20 s) leads to a grid of 374 knots at 80 s. When coverage is poorer (for periods of 20 s and shorter), the grid covers a reduced area (e.g., 351 knots at 20 s). Each dispersion curve yields the average phase velocity along the path linking the

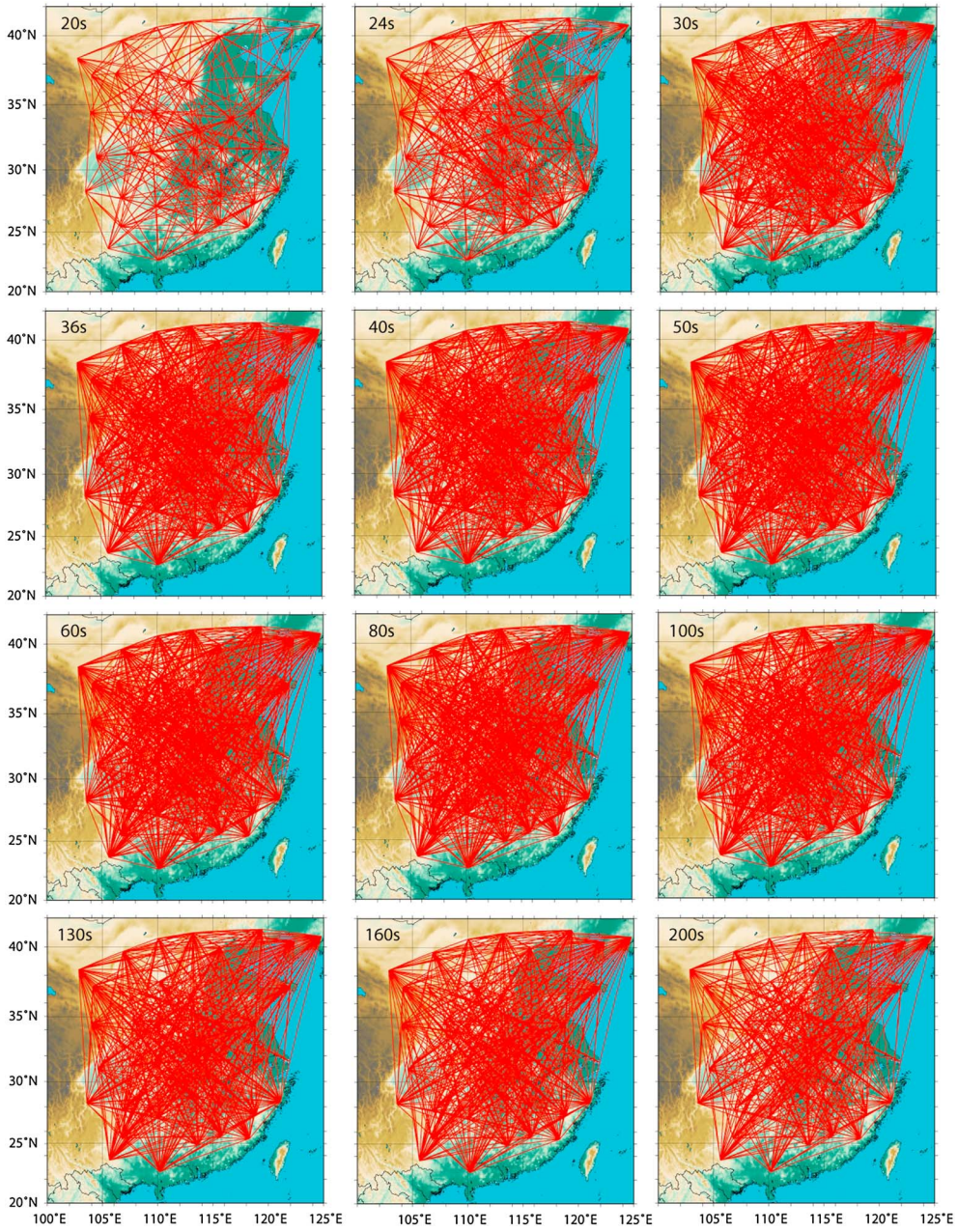


**Figure 8.** Paths used to constrain specific periods. From top left to bottom right are 20, 24, 30, 36, 40, 50, 60, 80, 100, 130, 160, and 200 s.

two stations as a function of period, and the total average velocity anomaly along this path may be written as the integral of local anomalies at each grid knot sampled by the given path:

$$\delta\bar{C}_i = \int_{\varphi}\int_{\theta} K_i(\varphi,\theta)\,\delta C(\varphi,\theta)\,\mathrm{d}\theta\,\mathrm{d}\varphi\,, \tag{5}$$

where the local anomalies $\delta C(\varphi,\theta)$ are weighted with respect to the sensitivity kernels $K_i(\varphi,\theta)$. The kernel provides the contribution at each knot on a specific path to the total velocity anomaly [*Lebedev and Van Der Hilst*, 2008]. The averaged velocities obtained from the dispersion curves are averaged for each period, and the inversion is performed to obtain the velocity perturbations relative to the regional average model. Note that inversion is performed independently at each period; i.e., for each selected period we define a set of linear equations (one for each path available at this period) by discretizing equation (5). We use the LSQR (least square for large sparse system) method [*Paige and Saunders*, 1982] to solve this

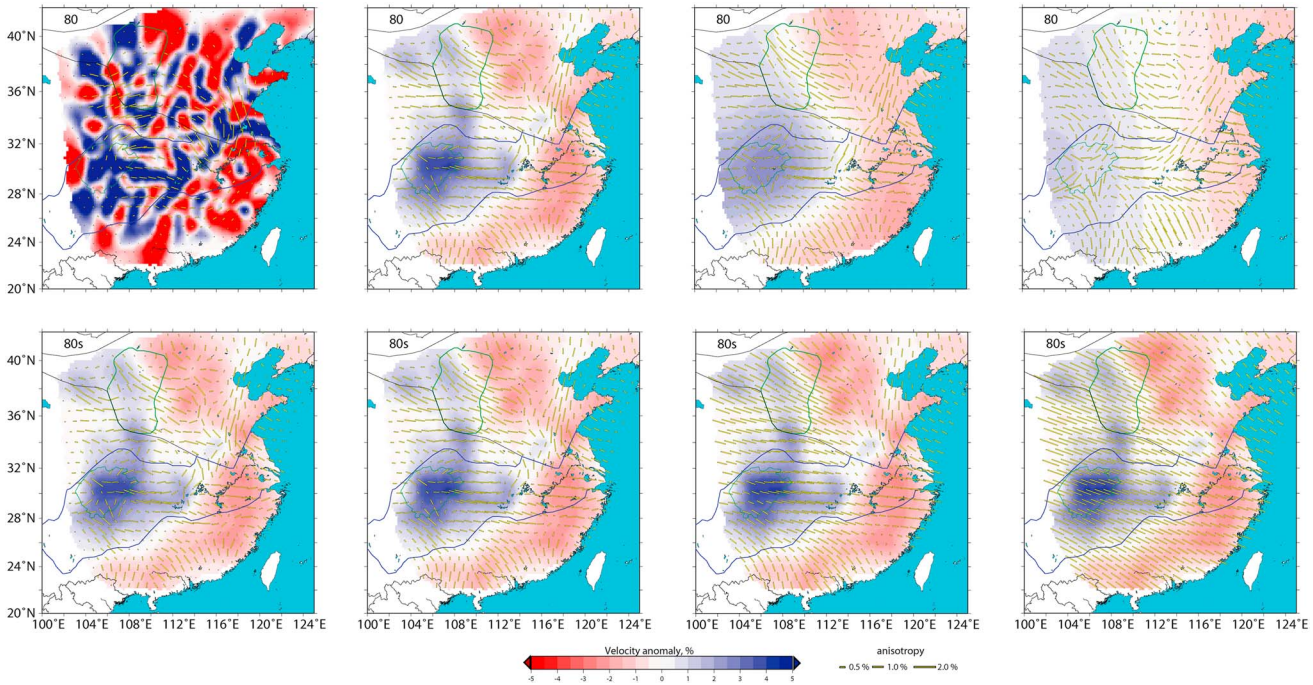


**Figure 9.** Effects of smoothing. The model has been calculated for a specific period of 80 s with increasing smoothing values from left to right for both (top) isotropic and (bottom) anisotropic components; all others parameters remain constant during the inversion process.

set of equations with both norm damping and lateral smoothing. Lateral smoothing is controlled by two damping parameters, which minimize the first and second spatial derivatives of velocity anomalies, respectively. Parameters for damping and smoothing are determined from trade-off curves. The amounts of damping and smoothing are different at different periods and are applied independently on isotropic and anisotropic terms. This method provides an effective mechanism (although not completely objective) to find the compromise between the smoothness of the model and its ability to explain the data. Resolution is mainly controlled not only by the cumulative sensitivity of the available data to isotropic and anisotropic perturbations within the medium but also by additional a priori constraints such as norm damping and smoothing. Here we discuss the influence of the latter two on the properties of the resulting model. Lateral smoothing penalizes the difference between the anomaly at a knot and the average of the anomalies at its neighboring knots by minimizing the first and second spatial derivatives of velocity anomalies. The lateral smoothing weight is set up independently for each period. We apply a stronger smoothing with decreasing path coverage. Figure 9 demonstrates the effect of smoothing on the resulting velocity model at a period of 80 s. If the smoothing weight is too low (Figure 9, left), small-scale artifacts may appear in the regions with poorer data coverage (i.e., at the border of the model). If the smoothing weight is instead too high, information on small-scale features is lost (Figure 9, right). Therefore, we imposed a smoothing weight large enough in order to avoid artifacts yet still allow the resolution of small-scale anomalies. Figure 9 also shows that the anisotropic pattern remains mostly unchanged, indicating the robustness of the inversion. We conducted similar tests for the anisotropic part (Figure 9, bottom).

### 2.4. Resolution Tests

To test the robustness of the dominant structures imaged by our models, we performed a series of synthetic tests (Figure 10). Simple input test models are first created with representative patterns for both isotropic and anisotropic anomalies. In the resolution tests, we first assume a synthetic model and expand it on the grid used in the tomography. We then multiply this model vector with the matrix that is used in the inversion of the real data and relates the data to the tomographic model. This result in a synthetic data vector; we then invert using the same regularization scheme as that used for the inversion of the real data. This allows testing for the reconstruction of both isotropic and anisotropic patterns. The retrieval of the anomalies should display correct amplitudes and locations. The anisotropic features should be retrieved with consistent directions and amplitudes. Distortions in the output models may result from several sources, but

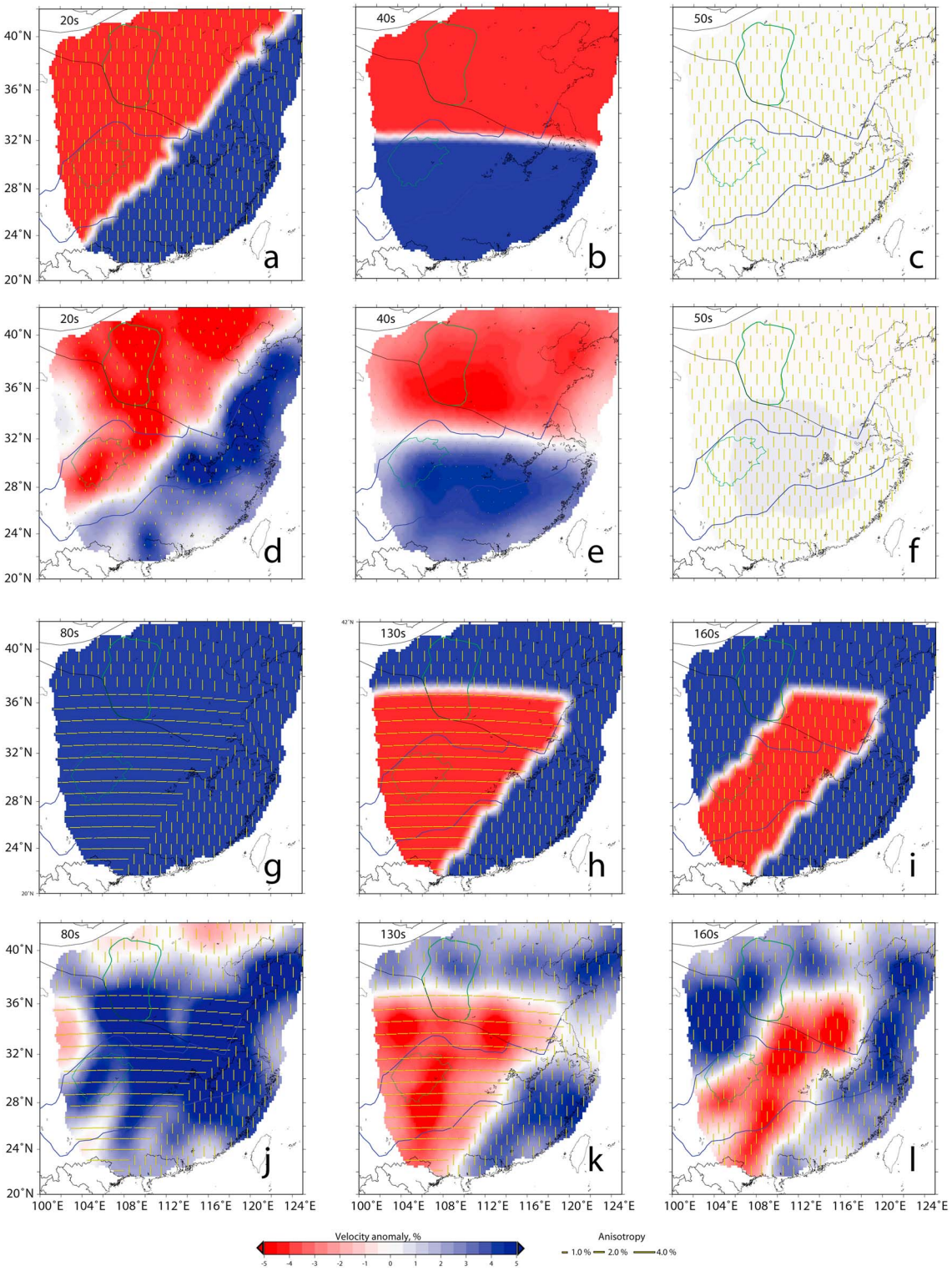


**Figure 10.** Resolution tests. Test models at periods of (a) 20 s, (b) 40 s, (c) 50 s, (g) 80 s, (h) 130 s, and (i) 160 s, and (d, f, j, and l) reconstructed models for respective periods. The reconstructions are performed to test the retrieval of both isotropic and anisotropic structures.

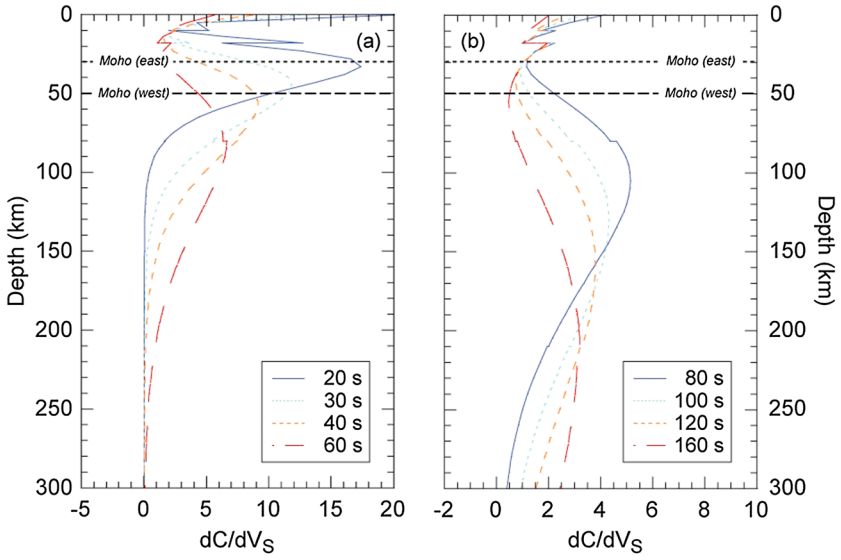


**Figure 11.** (a and b) Sensitivity of the Rayleigh wave phase velocity in function of depth, for selected periods.

mainly a lack of lateral resolution and leakage between isotropic and anisotropic terms (Figure 10). To evaluate the leakage between isotropic and anisotropic terms [*Darbyshire and Lebedev*, 2009; *Fry et al.*, 2010], we define three synthetic models in which isotropic and anisotropic anomalies are either constant throughout the region, or set to zero (Figures 10b, 10c, and 10g). The retrieved models (Figures 10e, 10f, and 10j) indicate that the leaking between isotropic and anisotropic terms is small. In particular, the isotropic patterns are retrieved for all periods with low lateral variations (Figure 10e). In regions with denser data coverage (between 20 and 160 s) some artifacts appear in the isotropic part. Note that these artifacts mostly occur at peripheral knots. These regions should thus be interpreted with caution, due to the possible small-scale artifacts and perturbations induced by possible errors in the data. Similarly, the input anisotropic structure (Figure 10c) is properly retrieved (Figure 10f). Inversion result shows only small deviation between input and output models both in the azimuth of fast direction and in amplitude, and the output model did not show substantial isotropic perturbations. To test whether specific isotropic and anisotropic structures can be geographically well resolved, we define two input models in which the isotropic and anisotropic distributions are more complex with tilted boundaries (Figures 10h, 10i, 10k, and 10l). The resolution tests presented here addressed the coverage given by the data and did not include errors in the data. Given the substantial redundancy of our coverage, provided by the hundreds of crossing paths, random errors are unlikely to have any significant impact on the main patterns seen in our results.

## 3. Results

We obtained variations in Rayleigh wave phase velocity anomaly with the location and period. Because Rayleigh waves at different periods sample different depth ranges, variations of Rayleigh wave phase velocity with period are related to vertical variations in shear wave velocity anomalies.

Our models are discussed in term of periods, but the frequencies can be related to depth by means of sensitivity kernels, displayed in Figure 11. Figure 11a is focused on the shorter periods (20–60 s). At 20 s, the Rayleigh waves samples a region between 10 and 80 km depth, with a maximum sensitivity around 30 km. By contrast, at 30 s, the Rayleigh waves samples a region between 20 and 100 km depth, with a maximum sensitivity around 40 km. Figure 11b is focused on longer periods (80–160 s). Rayleigh waves at a period of 100 s sample the depth range between 50 and 250 km, with a maximal sensitivity around 130 km. Using the kernels, it is possible to link the periods with depth. In this paper we do not relate dispersion curves to $V_s$ depth profiles quantitatively by means of inversion of the data [e.g., *Endrun et al.*, 2008; *Agius and Lebedev*, 2013], which is to be the focus of future work, but highlight the major isotropic and anisotropic heterogeneity patterns already apparent from phase velocity maps.

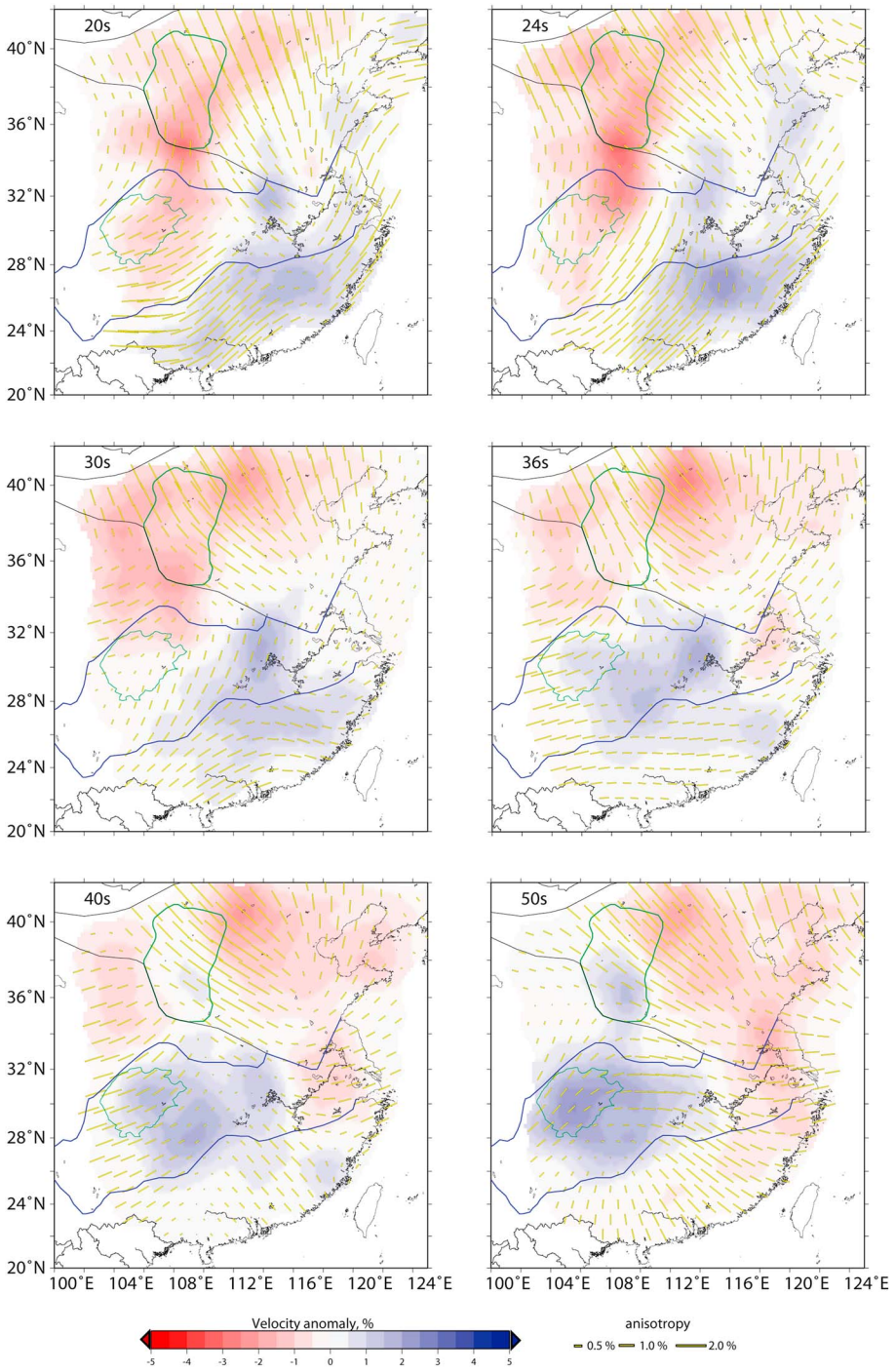


**Figure 12.** Isotropic and azimuthally anisotropic phase velocity maps for specific periods. From top left to bottom right are 20, 24, 30, 36, 40, and 50 s.

### 3.1. Isotropic Variations

In the period range of 20–30 s, the isotropic structure (Figure 12) is dominated by a northwest-southeast dichotomy. We observe fast velocity anomalies of up to 2% relative to the regional average velocity in the southeastern part of the model, corresponding roughly to the Cathaysia Unit, and low-velocity anomalies of up to −3% in the northwest, covering the Ordos Basin, the western part of the Sino-Korean Craton, and part of the plains and uplifted blocks. All these units comprise the northern tectonic block. Around 30–36 s, the isotropic pattern changes, with fast velocity migrating from the Cathaysia Unit toward the Yangtze

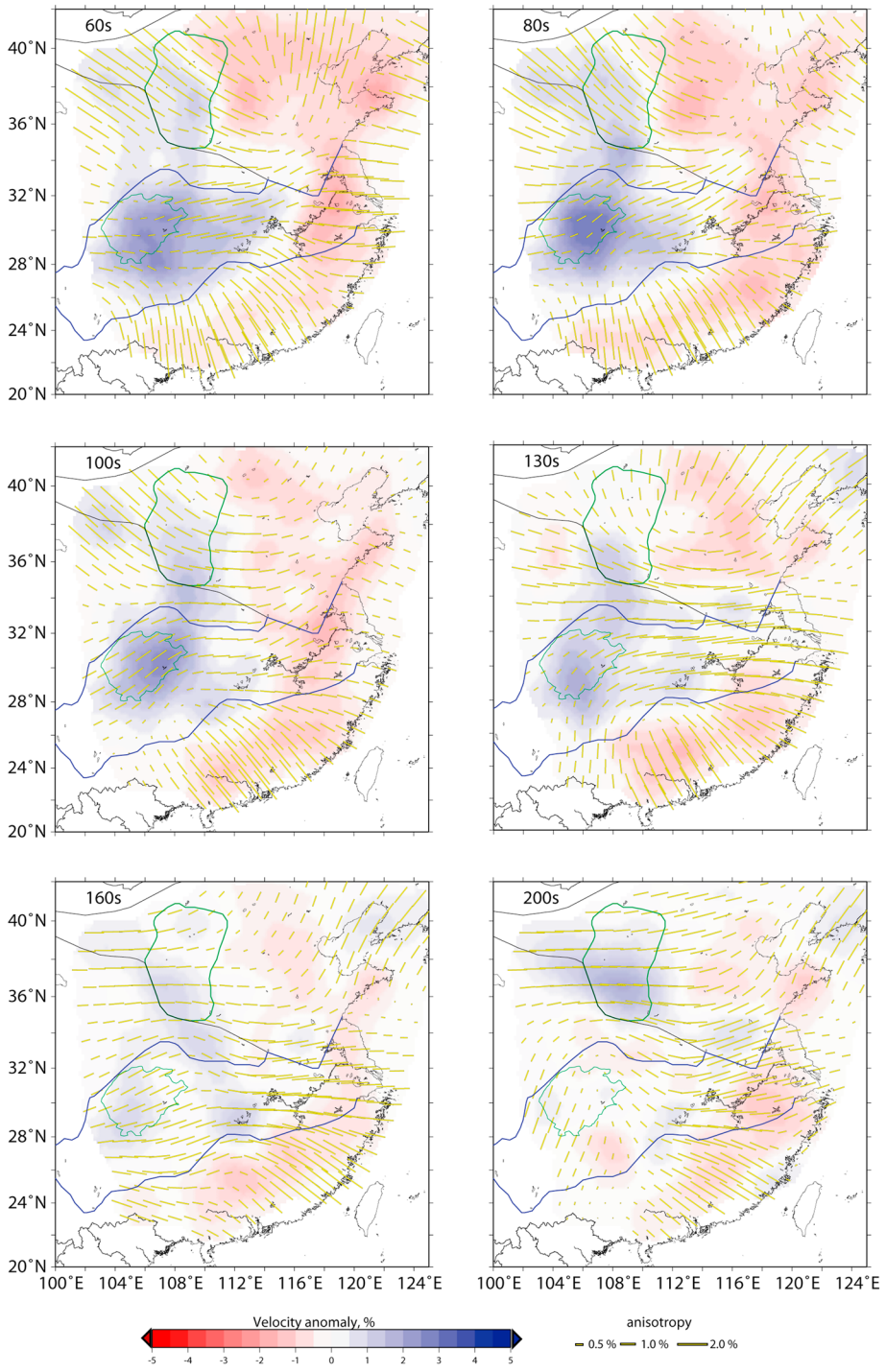


**Figure 13.** Isotropic and azimuthally anisotropic phase velocity maps for specific periods. From top left to bottom right are 60, 80, 100, 130, 160, and 200 s.

Craton. Between 30 and 100 s, the dominant feature is a dichotomy between the faster than average western Yangtze Craton and the slower than average eastern North China Craton. The Cathaysia Unit, in the southeastern part of our model is characterized by small anomalies (1% and less), faster than average in the period range 36–50 s and slower in the period range 60–100 s.

Our model shows substantial variations within each unit. Within the Yangtze Craton, the Sichuan Basin is faster than the surroundings at periods of 50 to 100 s (Figures 12 and 13). Within the North China Craton, the

main high-velocity anomaly is seen beneath the southern part of the Ordos Basin, which appears as faster than average at 50 s period and longer. The dominant isotropic pattern is thus a roughly E-W dichotomy. This pattern is observed up to about 100 s period.

At periods of 130 s and longer (Figure 13), the isotropic structure changes again and is progressively dominated by short-wavelength anomalies. At periods of 160 s and longer, corresponding to the asthenospheric mantle, we observe isotropic anomalies of shorter wavelength (typically a few hundreds of kilometers) and the model tends to become more homogeneous (the amplitudes of the anisotropy is smaller) at those longer periods. Note that the amplitude of the isotropic anomalies slowly decreases with increasing period, with anomalies of 1% and less at 160 s and longer periods.

### 3.2. The $2\psi$ Anisotropic Variations

Our anisotropic model is displayed together with the isotropic one in Figures 12 and 13 for the same periods. At 20 s period, corresponding to the midcrust, we observe four main regions with different anisotropic patterns. Beneath the North China Craton, anisotropy is strong with an amplitude of up to 2% and a NNW-SSE direction of fast propagation. Beneath Yangtze Craton, anisotropy strongly varies with the location, both in amplitude and direction of fast propagation. In the western part of the craton, we observe moderate anisotropy (1–1.5%) with SW-NE direction of fast propagation, whereas anisotropy is weak in its east central part. In the western part of the model (beneath Tibet), anisotropy is moderate (up to 1%), with a N-S direction of fast propagation. Near the southern border of our model, beneath Cathaysia, we see substantial anisotropy, with amplitude decreasing from 2% at 20 s to 1% at 30 s, and a roughly SW-NE direction of fast propagation. This pattern extends northward in the Yangtze Craton.

The strong NNW-SSE anisotropy observed in the Sino-Korean Craton persists up to 50 s period but changes at periods between 60 and 100 s. In this period range, anisotropy strongly varies in amplitude and direction within the Sino-Korean Craton. In its western part, beneath the Ordos Basin, it remains strong with NNW-SSE fast direction, but in the eastern and northern parts, anisotropy is weak. By contrast, in Cathaysia, the anisotropy changes in the period range of 36–40 s. At 50 s, and up to 100 s, we see strong anisotropy with the directions of fast propagation roughly perpendicular to the coastline from NW-SE in the west to E-W in the east. This anisotropic pattern extends beneath the eastern part of the Yangtze Craton, characterized by low-velocity isotropic anomalies at these periods. In the western part of the Yangtze Craton, anisotropy is moderate (around 1%), with SW-NE direction of fast propagation, slowly turning to an E-W direction in the eastern part of the model. Starting around 120 s, the dominant anisotropic pattern is a 1–2% anisotropy with E-W direction of fast propagation, consistent with the absolute plate motion (APM) in this region [*DeMets et al.*, 1990, 1994]. Strong variations are still present, in particular beneath Cathaysia Unit where the direction of fast propagation remains NW-SE. Discrepancies also appear at the periphery of the model and might be related to poor coverage at these periods.

## 4. Discussion

### 4.1. Crustal Thickness

The models at 20–36 s periods sample primarily the crust, according to the sensitivity kernels (Figure 11). One of the dominant features in the isotropic part of our model is the low velocities beneath the sedimentary basins (Ordos and Sichuan) in northwest part of our model. This anomaly persists up to periods around 24 s. The high velocities beneath Cathaysia and the SE-NW dichotomy in the isotropic structure at periods of 20–36 s may originate from two combined effects. The primary cause is likely to be the known crustal thickening toward the northwest. This is consistent with previous observations and crustal models of mainland China [*Zheng et al.*, 2008; *Sun et al.*, 2010; *Zhou et al.*, 2012] as well as models at larger scale [*Bassin et al.*, 2000], receiver function analyses [*Chen et al.*, 2010], and gravity measurements [*Xu*, 2007], showing a crustal thickness of 30 km beneath Cathaysia and a thickening toward the northwest, reaching 60–70 km beneath Tibet [*Huang et al.*, 2009; *Jiang et al.*, 2013]. Additionally, the thermochemical structure of Cathaysia and other units may differ, in the crust and in the mantle. According to the tectosphere hypothesis [*Jordan*, 1975] regarding cratons in particular, chemical depletion (e.g., in iron) is required to balance the cooling of the lithosphere and to maintain the long-term stability of a craton. The presence of chemical heterogeneities, however, cannot be diagnosed on the basis of our Rayleigh wave model only. Such anomalies may be inferred from vertical profiles of relative density-to-shear-wave velocity anomalies [e.g., *Deschamps et al.*, 2001; *Van Gerven et al.*, 2004], or appropriate petrophysical inversions of surface waves data [e.g., *Khan et al.*, 2011; *Fullea et al.*, 2012; *Khan et al.*, 2013].

### 4.2. Yangtze Craton and Cathaysia

The boundary between the Yangtze Craton and the Cathaysia Unit is known from the geological record and its surface expression [*Chen et al.*, 1981; *He and Tsukuda*, 2003], indicated in Figures 12 and 13. The Jiangnan Belt stretches along the suture between the Yangtze Craton and the Cathaysia Unit [*Zhang et al.*, 2013].

At periods between 40 and 80 s (sampling the mantle lithosphere and, where the lithosphere is not very thick, the asthenosphere), the dominant structure is a strong change of velocity beneath the Jiangnan Belt (low velocities in the east and high velocities in the west) as seen in previous local-scale studies [*Zheng et al.*, 2008; *Sun et al.*, 2010; *Zhou et al.*, 2012]. The high velocities observed beneath the Yangtze Craton and low velocities beneath the Cathaysia Unit indicate the thicker lithosphere beneath the western and central Yangtze Craton. In contrast, in the eastern part of the Yangtze Craton, low velocities are found. This suggests that the mantle lithosphere east of 116°E is thin and no longer cratonic.

The layered azimuthal anisotropy beneath Cathaysia reveals different fabric within the lithosphere and asthenosphere. In the lithosphere (20–36 s periods) the fast directions are oriented NE-SW, roughly parallel to the present coastline and to the suture with the Yangtze Craton. This anisotropy is likely to indicate the frozen fabric created by the deformation of Cathaysia during and following its collision and suturing with the Yangtze Craton.

In the asthenosphere (periods longer than about 40 s), fast propagation directions beneath Cathaysia, as well as beneath eastern Yangtze Craton, are different, roughly perpendicular to the coastline. This fabric indicates the current asthenospheric flow, probably from beneath mainland China toward the east.

Cenozoic basalts that erupted near China's eastern coast display isotopic ratios typical of ocean-island basalts [e.g., *Flower et al.*, 1998; *Smith*, 1998], often associated with hot spot volcanism. In the southeast, in the vicinity of Hainan Island, a deep seismic velocity anomaly has been detected, with the volcanism there thus attributed to the Hainan Plume [*Lebedev and Nolet*, 2003; *Lei et al.*, 2009]. Elsewhere along the eastern coast, however, the volcanism is likely to have a shallower origin. *Morgan and Morgan* [2005] proposed that some of the Cenozoic intraplate volcanism in East Asia may be due to horizontal sublithospheric flow, driven by the "draining" of asthenosphere at the subduction zones to the east. Subducting slabs consume asthenospheric material by dragging down a thin layer of it, with the lost asthenosphere then replaced by means of sublithospheric flow from beneath Asia. In locations where the flow rises from beneath thicker continental lithosphere to beneath thinner lithosphere at the continent's margin, pressure-release melting, and volcanism can occur [*Thompson and Gibson*, 1991]. The veins of enriched rock within the mantle may melt preferentially (the "plums" in the terminology of the "plum pudding" geochemical mantle model [*Morris and Hart*, 1983; *Morgan and Morgan*, 1999]), with the resulting basaltic volcanism then similar to that observed at hot spots.

The azimuthal anisotropy that we map beneath eastern China at intermediate and long periods may thus indicate the eastward flow of the asthenosphere that has caused the Cenozoic intraplate volcanism along the coast.

### 4.3. North China Craton

High velocities found beneath Ordos and Sichuan Basins correspond to their deep cratonic keels. Fast velocities are found up to 100 or 130 s, suggesting that these keels extend at large depths (down to 200 km), which is consistent with shear wave speed tomographic models in the region [*Huang et al.*, 2009; *Jiang et al.*, 2013].

The structure of the crust and lithosphere beneath the North China Craton has been extensively studied (see *Zhai and Liu* [2003] for a review). *Zhang* [2012] proposed that the lithosphere beneath the NCC was removed by lithosphere folding, delamination, and dripping. The thinning of the lithosphere beneath NCC is known from Bouguer anomaly and heat flow measurements [*Griffin et al.*, 1998] and confirmed by isotopic analyses [*Xu*, 2001; *Zhang et al.*, 2002, 2013].

In our models, we map the eastern boundary of the preserved, stable lithosphere of both the Yangtze Craton in the South and the North China Craton in the north. East of the boundary, we observe a low-velocity region, with a thin lithosphere.

### 4.4. Local and Regional Features

Active faulting (Figure 1) indicates that the Sino-Korean Craton is now deformed more strongly than the Yangtze Craton. The Sino-Korean Craton has also experienced substantial deformation in the past, since its formation [*Menzies and Xu*, 1998]. Interestingly, in the period range of 20–100 s (corresponding to the lower crust and lithospheric mantle), we observe strong geographical variations of azimuthal anisotropy within the Sino-Korean Craton, both in the direction of fast propagation and in the amplitude. By contrast, azimuthal anisotropy is relatively homogeneous within much of the Yangtze Craton at most periods, with a small amplitude in the period range of 20–40 s. The $2\psi$ anisotropy pattern we observe between periods of 20 and 36 s can be related to the regional tectonics. Between the Ordos and Sichuan Basins, the orientation of the fast direction of propagation rotates to become NNE. The distinct lithospheric structure of this unit is seen in its lower isotropic-average velocity as well. Fast propagation directions observed at 50 s and longer are similar to those inferred from SKS splitting measurements [*Wüstefeld et al.*, 2009; *Bai et al.*, 2010]. However, one has to keep in mind that the SKS waves sample several layers along their path. Because the anisotropy we observe in this region varies with period (both in amplitude and direction of fast propagation), a detailed comparison between our Rayleigh wave anisotropy and the observed SKS measurements would require to invert our anisotropic models for 3-D shear wave anisotropy and vertically integrate through this 3-D model.

The border area between the two rigid blocks, the Ordos and Sichuan Basins, is a region with intense faulting (Figure 1). The faults do not penetrate the units, indicating that the border region between the two blocks is mechanically weaker than the blocks themselves. The anisotropic pattern observed in our model is consistent with not only the distribution of the surface faults around the basins with strong lateral and depth variations but also previous SKS splitting studies of this region [*Wüstefeld et al.*, 2009; *Bai et al.*, 2010; *Li et al.*, 2011]. However, the present strain within the blocks is low, so that the anisotropy is likely to be due to frozen fabric, created long ago. West of the Jiangnan Belt, the isotropic structure is dominated by short-wavelength (about 400 km) anomalies but is relatively homogeneous at larger scale. The anisotropy in the whole region has a roughly E-W axis of fast propagation in the shallow part but rotates to become consistent with the overall APM direction at longer periods. At long periods (160 s and longer), sampling the asthenosphere, the anisotropic pattern varies only slightly with location.

### 4.5. Comparison With Previous Studies

The boundary of the cratons have already been delineated by regional body wave tomography models [*Liang et al.*, 2004; *Huang and Zhao*, 2006; *Sun and Toksöz*, 2006; *Zhao et al.*, 2012]. These models clearly show an east-west dichotomy in their shallowest part, which can be related to the shorter-period structures in our surface wave models, with high velocities in the east and low velocities westward. This east-west dichotomy is often referred to as the north-south tectonic line [*He and Tsukuda*, 2003].

Models obtained from surface wave tomography [*Huang et al.*, 2009; *Jiang et al.*, 2013] and ambient noise tomography [*Zheng et al.*, 2008; *Sun et al.*, 2010; *Zhou et al.*, 2012] display high velocities in the southeast (beneath the Cathaysia Unit) at shallow depths and low velocities in the same region at greater depth, which is also consistent with our isotropic model. The shallowest part of our model display fast velocities beneath the NCC. This is in good agreement with previous gravity measurements [*Xu*, 2007]. The high velocities beneath the North China Craton are well correlated with the positive Bouguer anomalies found in the region, comforting the idea of the erosion of the lithosphere beneath the North China Craton.

SKS measurements (see *Wüstefeld et al.* [2009] for a review) are very dense in the studied region. Good agreement between the fast axis of polarization of the SKS measurements and the anisotropic part of our models are found. The SKS measurements seem mostly sensitive to the mantle deformation, as expected, but in some parts of the models, we also see a match between the crustal anisotropy and the SKS splitting results.

## 5. Conclusions

In this study, we have constructed anisotropic Rayleigh wave phase velocity maps for eastern China using broadband seismograms from the China National Seismic Network. The models we obtain at different periods reveal features changing both laterally and with period (i.e., reflecting shear wave speed changes with depth). Phase velocity changes are observed across the boundaries between tectonic units, such as between

the North China Craton, Yangtze Craton, and the Cathaysia Block. We also observe a sharp transition in seismic velocities at the border of the Tibetan Plateau.

The isotropic part of the model reveals clear differences in the lithospheric structure of the main units of the region, including not only the large-scale cratons (Yangtze and Sino-Korean) but also the smaller-scale basins within them (Ordos and Sichuan), defining their deep geometry. Lateral and vertical variations of azimuthal anisotropy provide more details on the tectonic evolution and current mantle dynamics beneath the region. The change in both isotropic and anisotropic perturbations occurs beneath the Jiangnan Belt, related to the lithospheric suture between the Yangtze Craton and Cathaysia Units. Thick cratonic lithosphere underlies the western part of the Yangtze Craton. East of 115–116°E, however, the Yangtze Craton lithosphere is thin, with no deep cratonic root present. Azimuthal anisotropy in the asthenosphere beneath Cathaysia and eastern Yangtze Craton indicates coast-perpendicular mantle flow. This flow from beneath China's thick continental lithosphere toward the margins and the subduction zones to the east may be the basic cause of the intraplate basaltic volcanism observed along the eastern coast of China.

**Acknowledgments**

This work was funded by a Career Development Award (AS-098-CDA-M02) of Academia Sinica (Taipei, Taiwan) and the National Science Council of Taiwan under grants NSC-101-2116-M-001-035 and NSC-101-2116-M-001-001-MY3. S. Lebedev acknowledges partial support from the Science Foundation Ireland grant 09/RFP/GEO2550. Waveform data for this study are provided by Data Management Centre of China National Seismic Network at the Institute of Geophysics, China Earthquake Administration [*Zheng et al.*, 2010]. Figures were generated with the Generic Mapping Tools [*Wessel and Smith*, 1995].

## References

Agius, M. R., and S. Lebedev (2013), Tibetan and Indian lithospheres in the upper mantle beneath Tibet: Evidence from broadband surface-wave dispersion, *Geochem. Geophys. Geosyst.*, *14*, 4260–4281, doi:10.1002/ggge.20274.

Avouac, J.-P., and P. Tapponnier (1993), Kinematic model of active deformation in central Asia, *Geophys. Res. Lett.*, *20*(10), 895–898.

Bai, L., H. Kawakatsu, and Y. Morita (2010), Two anisotropic layers in central orogenic belt of North China craton, *Tectonophysics*, *494*(1-2), 138–148.

Bassin, C., G. Laske, and G. Masters (2000), The current limits of resolution for surface wave tomography in North America, *Eos Trans. AGU*, *81*(48), Fall Meet. Suppl., Abstract F897.

Bijwaard, H., W. Spakman, and E. R. Engdahl (1998), Closing the gap between regional and global travel time tomography, *J. Geophys. Res.*, *103*(B12), 30,055–30,078.

Bird, P. (2003), An updated digital model of plate boundaries, *Geochem. Geophys. Geosyst.*, *4*(3), 1027, doi:10.1029/2001GC000252.

Chen, J., and B. M. Jahn (1998), Crustal evolution of southeastern China: Nd and Sr isotopic evidence, *Tectonophysics*, *284*(1-2), 101–133.

Chen, J., H. Zhang, Y. Xing, and G. Ma (1981), On the upper Precambrian (Sinian Suberathem) in China, *Precambrian Res.*, *15*(3-4), 207–228.

Chen, Y., F. Niu, R. Liu, Z. Huang, H. Tkalčić, L. Sun, and W. Chan (2010), Crustal structure beneath China from receiver function analysis, *J. Geophys. Res.*, *115*, B03307, doi:10.1029/2009JB006386.

Darbyshire, F. A., and S. Lebedev (2009), Rayleigh wave phase-velocity heterogeneity and multilayered azimuthal anisotropy of the Superior Craton, Ontario, *Geophys. J. Int.*, *176*(1), 215–234.

DeMets, C., R. Gordon, D. Argus, and S. Stein (1990), Current plate motions, *Geophys. J. Int.*, *101*(2), 425–478.

DeMets, C., R. Gordon, D. Angus, and S. Stein (1994), Effect of recent revisions to the geomagnetic reversal time scale on estimates of current plate motions, *Geophys. Res. Lett.*, *21*(20), 2191–2194.

Deng, Q., P. Zhang, Y. Ran, X. Yang, W. Min, and Q. Chu (2003), Basic characteristics of active tectonics of China, *Sci. China Ser. D: Earth Sci.*, *46*(4), 356–372.

Deschamps, F., R. Snieder, and J. Trampert (2001), The relative density-to-shear velocity scaling in the uppermost mantle, *Phys. Earth Planet. Inter.*, *124*(3), 193–212.

Deschamps, F., S. Lebedev, T. Meier, and J. Trampert (2008a), Azimuthal anisotropy of Rayleigh-wave phase velocities in the East-Central United States, *Geophys. J. Int.*, *173*, 827–843.

Deschamps, F., S. Lebedev, T. Meier, and J. Trampert (2008b), Stratified seismic anisotropy reveals past and present deformation beneath the east-central United States, *Earth Planet. Sci. Lett.*, *274*(3), 489–498.

Endrun, B., T. Meier, S. Lebedev, M. Bohnhoff, G. Stavrakakis, and H.-P. Harjes (2008), S velocity structure and radial anisotropy in the Aegean region from surface wave dispersion, *Geophys. J. Int.*, *174*(2), 593–616.

Endrun, B., S. Lebedev, T. Meier, C. Tirel, and W. Friederich (2011), Complex layered deformation within the Aegean crust and mantle revealed by seismic anisotropy, *Nat. Geosci.*, *4*(3), 203–207.

Flower, M., K. Tamaki, and N. Hoang (1998), Mantle extrusion: A model for dispersed volcanism and DUPAL-like asthenosphere in East Asia and the western Pacific, in *Mantle Dynamics and Plate Interactions in East Asia, Geodyn. Ser.*, vol. 27, edited by M. F. J. Flower et al., pp. 67–88, AGU, Washington, D. C.

Friederich, W. (2003), The S-velocity structure of the East Asian mantle from inversion of shear and surface waveforms, *Geophys. J. Int.*, *153*(1), 88–102.

Fry, B., F. Deschamps, E. Kissling, L. Stehly, and D. Giardini (2010), Layered azimuthal anisotropy of Rayleigh wave phase velocities in the European Alpine lithosphere inferred from ambient noise, *Earth Planet. Sci. Lett.*, *297*(1), 95–102.

Fullea, J., S. Lebedev, M. Agius, A. Jones, and J. C. Afonso (2012), Lithospheric structure in the Baikal-central Mongolia region from integrated geophysical-petrological inversion of surface-wave data and topographic elevation, *Geochem. Geophys. Geosyst.*, *13*, Q0AK09, doi:10.1029/2012GC004138.

Griffin, W., Z. Andi, S. O'reilly, and C. Ryan (1998), Phanerozoic evolution of the lithosphere beneath the Sino-Korean Craton, in *Mantle Dynamics and Plate Interactions in East Asia, Geodyn. Ser.*, vol. 27, edited by M. F. J. Flower et al., pp. 107–126, AGU, Washington, D. C.

He, H., and E. Tsukuda (2003), Recent progresses of active fault research in China, *J. Geogr.*, *112*(4), 489–520.

Huang, J., and D. Zhao (2006), High-resolution mantle tomography of China and surrounding regions, *J. Geophys. Res.*, *111*, B09305, doi:10.1029/2005JB004066.

Huang, Z., H. Li, Y. Zheng, and Y. Peng (2009), The lithosphere of north China craton from surface wave tomography, *Earth Planet. Sci. Lett.*, *288*(1-2), 164–173.

Inoue, H., Y. Fukao, K. Tanabe, and Y. Ogata (1990), Whole mantle P-wave travel time tomography, *Phys. Earth Planet. Inter.*, *59*(4), 294–328.

Jiang, M., Y. Ai, L. Chen, and Y. Yang (2013), Local modification of the lithosphere beneath the central and western North China Craton: 3-D constraints from Rayleigh wave tomography, *Gondwana Res.*, *24*, 849–864.

Jordan, T. H. (1975), The continental tectosphere, *Rev. Geophys.*, *13*(3), 1–12.

Khan, A., A. Zunino, and F. Deschamps (2011), The thermo-chemical and physical structure beneath the North American continent from Bayesian inversion of surface-wave phase velocities, *J. Geophys. Res.*, *116*, B09304, doi:10.1029/2011JB008380.

Khan, A., A. Zunino, and F. Deschamps (2013), Upper mantle compositional variations and discontinuity topography imaged beneath Australia from Bayesian inversion of surface-wave phase velocities and thermochemical modeling, *J. Geophys. Res. Solid Earth*, *118*, 5285–5306, doi:10.1002/jgrb.50304.

Knapmeyer-Endrun, B., F. Krüger, C. Legendre, and W. Geissler (2013), Tracing the influence of the Trans-European Suture Zone into the mantle transition zone, *Earth Planet. Sci. Lett.*, *363*, 73–87.

Knopoff, L. (1972), Observation and inversion of surface-wave dispersion, *Tectonophysics*, *13*, 497–519.

Lebedev, S., and G. Nolet (2003), Upper mantle beneath Southeast Asia from S-velocity tomography, *J. Geophys. Res.*, *108*(B1), 2048, doi:10.1029/2000JB000073.

Lebedev, S., and R. D. Van Der Hilst (2008), Global upper-mantle tomography with the automated multimode inversion of surface and S-wave forms, *Geophys. J. Int.*, *173*(2), 505–518.

Lebedev, S., G. Nolet, T. Meier, and R. Van Der Hilst (2005), Automated multimode inversion of surface and S-waveforms, *Geophys. J. Int.*, *162*(3), 951–964.

Lebedev, S., T. Meier, and R. Van Der Hilst (2006), Asthenospheric flow and origin of volcanism in the Baikal Rift area, *Earth Planet. Sci. Lett.*, *249*(3), 415–424.

Lebedev, S., J. Boonen, and J. Trampert (2009), Seismic structure of Precambrian lithosphere: New constraints from broad-band surface-wave dispersion, *Lithos*, *109*(1), 96–111.

Legendre, C. P., T. Meier, S. Lebedev, W. Friederich, and L. Viereck-Götte (2012), A shear-wave velocity model of the European upper mantle from automated inversion of seismic shear and surface waveforms, *Geophys. J. Int.*, *191*(1), 282–304.

Lei, J., D. Zhao, B. Steinberger, B. Wu, F. Shen, and Z. Li (2009), New seismic constraints on the upper mantle structure of the Hainan Plume, *Phys. Earth Planet. Inter.*, *173*(1), 33–50.

Li, C., R. D. Van Der Hilst, and M. N. Toksöz (2006), Constraining P-wave velocity variations in the upper mantle beneath Southeast Asia, *Phys. Earth Planet. Inter.*, *154*(2), 180–195.

Li, J., X. Wang, and F. Niu (2011), Seismic anisotropy and implications for mantle deformation beneath the NE margin of the Tibet Plateau and Ordos Plateau, *Phys. Earth Planet. Inter.*, *189*(3-4), 157–170.

Li, Y., and Y. Yang (2011), Gravity data inversion for the lithospheric density structure beneath north China craton from EGM 2008 model, *Phys. Earth Planet. Inter.*, *189*(1-2), 9–26.

Li, Z.-X., X.-H. Li, S.-L. Chung, C.-H. Lo, X. Xu, and W.-X. Li (2012), Magmatic switch-on and switch-off along the South China continental margin since the Permian: Transition from an Andean-type to a Western Pacific-type plate boundary, *Tectonophysics*, *532-535*, 271–290.

Liang, C., X. Song, and J. Huang (2004), Tomographic inversion of Pn travel times in China, *J. Geophys. Res.*, *109*, B11304, doi:10.1029/2003JB002789.

Lü, Y., Z. Zhang, S. Pei, E. Sandvol, T. Xu, and X. Liang (2013), 2.5-dimensional tomography of uppermost mantle beneath Sichuan-Yunnan and surrounding regions, *Tectonophysics*, doi:10.1016/j.tecto.2013.03.008, in press.

Ma, Y., and H. Zhou (2007), Crustal thicknesses and Poisson's ratios in China by joint analysis of teleseismic receiver functions and Rayleigh wave dispersion, *Geophys. Res. Lett.*, *34*, L12304, doi:10.1029/2007GL029848.

Meier, T., K. Dietrich, B. Stöckhert, and H.-P. Harjes (2004), One-dimensional models of shear-wave velocity for the eastern Mediterranean obtained from the inversion of Rayleigh wave phase velocities and tectonic implications, *Geophys. J. Int.*, *156*, 45–58.

Meng, L., Z.-X. Li, H. Chen, X.-H. Li, and X.-C. Wang (2012), Geochronological and geochemical results from Mesozoic basalts in southern South China block support the flat-slab subduction model, *Lithos*, *132-133*, 127–140.

Menzies, M. A., and Y. Xu (1998), Geodynamics of the North China Craton, in *Mantle Dynamics and Plate Interactions in East Asia*, edited by F. J. Flower et al., pp. 155–165, AGU, Washington, D. C.

Montagner, J.-P., and T. Tanimoto (1991), Global upper mantle tomography of seismic velocities and anisotropies, *J. Geophys. Res.*, *962*, 20,337–20,351.

Morgan, P., and W. Morgan (1999), Two-stage melting and the geochemical evolution of the mantle: A recipe for mantle plum-pudding, *Earth Planet. Sci. Lett.*, *170*(3), 215–239.

Morgan, W., and P. Morgan (2005), Volcanism due to horizontal sublithospheric flow, paper presented at 4th Deep Earth: Theory, Experiment and Observation Research Conference, Lithosphere-Asthenosphere Interaction, Frejus, France.

Morris, J., and S. Hart (1983), Isotopic and incompatible element constraints on the genesis of island arc volcanics from Cold Bay and Amak Island, Aleutians, and implications for mantle structure, *Geochim. Cosmochim. Acta*, *47*(11), 2015–2030.

Paige, C. C., and M. A. Saunders (1982), LSQR: An algorithm for sparse linear equations and sparse least squares, *ACM Trans. Math. Software*, *8*(1), 43–71.

Pei, S., J. Zhao, Y. Sun, Z. Xu, S. Wang, H. Liu, C. Rowe, M. Toksöz, and X. Gao (2007), Upper mantle seismic velocities and anisotropy in China determined through Pn and Sn tomography, *J. Geophys. Res.*, *112*, B05312, doi:10.1029/2006JB004409.

Polat, G., S. Lebedev, P. Readman, B. O'Reilly, and F. Hauser (2012), Anisotropic Rayleigh-wave tomography of Ireland's crust: Implications for crustal accretion and evolution within the Caledonian Orogen, *Geophys. Res. Lett.*, *39*, L04302, doi:10.1029/2012GL051014.

Sato, Y. (1955), Analysis of dispersed surface waves by means of Fourier transform, I, *Bull. Earthquake Res. Tokyo Univ.*, *33*(1), 33–48.

Schaeffer, A., and S. Lebedev (2013), Global shear speed structure of the upper mantle and transition zone, *Geophys. J. Int.*, *194*(1), 417–449.

Schwab, F., and L. Knopoff (1970), Surface-wave dispersion computations, *Bull. Seismol. Soc. Am.*, *60*(2), 321–344.

Smith, A. D. (1998), The geodynamic significance of the DUPAL anomaly in Asia, in *Mantle Dynamics and Plate Interactions in East Asia, Geodyn. Ser.*, vol. 27, edited by M. F. J. Flower et al., pp. 89–105, AGU, Washington, D. C.

Sun, X., X. Song, S. Zheng, Y. Yang, and M. Ritzwoller (2010), Three dimensional shear wave velocity structure of the crust and upper mantle beneath China from ambient noise surface wave tomography, *Earthquake Sci.*, *23*, 449–463.

Sun, Y., and M. N. Toksöz (2006), Crustal structure of China and surrounding regions from *P* wave traveltime tomography, *J. Geophys. Res.*, *111*, B03310, doi:10.1029/2005JB003962.

Tapponnier, P., G. Peltzer, and R. Armijo (1986), On the mechanics of the collision between India and Asia, in *Collision Tectonics*, vol. 19, pp. 113–157, Geol. Soc. Spec. Publ., London, U. K.

Trampert, J., and J. H. Woodhouse (2003), Global anisotropic phase-velocity maps for fundamental mode surface waves between 40 and 150 s, *Geophys. J. Int.*, *154*(1), 154–165.

Thompson, R., and S. A. Gibson (1991), Subcontinental mantle plumes, hotspots and pre-existing thinspots, *J. Geol. Soc.*, *148*(6), 973–977.

Van Gerven, L., F. Deschamps, and R. D. Van Der Hilst (2004), Geophysical evidence for chemical variations in the Australian continental mantle, *Geophys. Res. Lett.*, *31*, L17607, doi:10.1029/2004GL020307.
Wang, Z., and F. A. Dahlen (1995), Spherical-spline parameterization of three-dimensional Earth models, *Geophys. Res. Lett.*, *22*(22), 3099–3102.
Wessel, P., and W. H. Smith (1995), New version of the generic mapping tools, *Eos Trans. AGU*, *76*(33), 329–336.
Wüstefeld, A., G. Bokelmann, G. Barruol, and J. Montagner (2009), Identifying global seismic anisotropy patterns by correlating shear-wave splitting and surface-wave data, *Phys. Earth Planet. Inter.*, *176*(3), 198–212.
Xie, J., M. H. Ritzwoller, W. Shen, Y. Yang, Y. Zheng, and L. Zhou (2013), Crustal radial anisotropy across Eastern Tibet and the Western Yangtze craton, *J. Geophys. Res. Solid Earth*, *118*, 4226–4252, doi:10.1002/jgrb.50296.
Xu, Y.-G. (2001), Thermo-tectonic destruction of the Archaean lithospheric keel beneath the Sino-Korean Craton in China: Evidence, timing and mechanism, *Phys. Chem. Earth Part A*, *26*(9), 747–757.
Xu, Y.-G. (2007), Diachronous lithospheric thinning of the north China craton and formation of the Daxin'anling-Taihangshan gravity lineament, *Lithos*, *96*(1–2), 281–298.
Yao, H., R. D. Van Der Hilst, and M. V. De Hoop (2006), Surface-wave array tomography in SE Tibet from ambient seismic noise and two-station analysis–I. Phase-velocity maps, *Geophys. J. Int.*, *166*(2), 732–744.
Yao, W.-H., Z.-X. Li, W.-X. Li, X.-C. Wang, X.-H. Li, and J.-H. Yang (2012), Post-kinematic lithospheric delamination of the Wuyi-Yunkai orogen in South China: Evidence from ca. 435 Ma high-Mg basalts, *Lithos*, *154*, 115–129.
Yin, A., and T. Harrison (2000), Geologic evolution of the Himalayan-Tibetan orogen, *Annu. Rev. Earth Planet. Sci.*, *28*(1), 211–280.
Yuan, H., and B. Romanowicz (2010), Lithospheric layering in the North American craton, *Nature*, *466*(7310), 1063–1068.
Zhai, M., and W. Liu (2003), Palaeoproterozoic tectonic history of the North China Craton: A review, *Precambrian Res.*, *122*(1), 183–199.
Zhang, H.-F., M. Sun, X.-H. Zhou, W.-M. Fan, M.-G. Zhai, and J.-F. Yin (2002), Mesozoic lithosphere destruction beneath the North China Craton: Evidence from major-, trace-element and Sr–Nd–Pb isotope studies of Fangcheng basalts, *Contrib. Mineral. Petrol.*, *144*(2), 241–254.
Zhang, K.-J. (2012), Destruction of the North China craton: Lithosphere folding-induced removal of lithospheric mantle?, *J. Geodyn.*, *53*, 8–17.
Zhang, Q., E. Sandvol, J. Ni, Y. Yang, and Y. J. Chen (2011), Rayleigh wave tomography of the northeastern margin of the Tibetan Plateau, *Earth Planet. Sci. Lett.*, *304*(1-2), 103–112.
Zhang, Y., Y. Wang, H. Geng, Y. Zhang, W. Fan, and H. Zhong (2013), Early neoproterozoic (850 Ma) back-arc basin in the Central Jiangnan Orogen (Eastern South China): Geochronological and petrogenetic constraints from meta-basalts, *Precambrian Res.*, *231*, 325–342.
Zhao, G., S. Wilde, P. Cawood, and M. Sun (2001), Archean blocks and their boundaries in the North China Craton: Lithological, geochemical, structural and P/T path constraints and tectonic evolution, *Precambrian Res.*, *107*(1), 45–73.
Zhao, L., R. M. Allen, T. Zheng, and R. Zhu (2012), High-resolution body wave tomography models of the upper mantle beneath Eastern China and the adjacent areas, *Geochem. Geophys. Geosyst.*, *13*, Q06007, doi:10.1029/2012GC004119.
Zheng, S., X. Sun, X. Song, Y. Yang, and M. H. Ritzwoller (2008), Surface wave tomography of China from ambient seismic noise correlation, *Geochem. Geophys. Geosyst.*, *9*, Q05020, doi:10.1029/2008GC001981.
Zheng, X.-F., Z.-X. Yao, J.-H. Liang, and J. Zheng (2010), The role played and opportunities provided by IGP DMC of China National Seismic Network in Wenchuan earthquake disaster relief and researches, *Bull. Seismol. Soc. Am.*, *100*(5B), 2866–2872.
Zhou, L., J. Xie, W. Shen, Y. Zheng, Y. Yang, H. Shi, and M. H. Ritzwoller (2012), The structure of the crust and uppermost mantle beneath South China from ambient noise and earthquake tomography, *Geophys. J. Int.*, *189*(3), 1565–1583.